ELSEVIER

Modeling a nanowire superlattice using the finite difference method in cylindrical polar coordinates

C. Galeriu [a], L.C. Lew Yan Voon [a,b,*], R. Melnik [b], M. Willatzen [b]

[a] *Department of Physics, Worcester Polytechnic Institute, 100 Institute Road, Worcester, MA 01609, USA*
[b] *Mads Clausen Institute, University of Southern Denmark, Grundtvigs Alle 150, DK-6400 Sønderborg, Denmark*

Abstract

A new procedure for handling periodic boundary conditions within the finite difference method and in cylindrical polar coordinates is presented and applied to modeling a nanowire superlattice. The method is compared for accuracy and efficiency with two other formulations of the same problem: the finite difference method applied to a finite number of unit cells, and the exact solution of the equivalent Kronig–Penney model. The technique is then shown to reproduce a novel physical state, and is applied to an embedded nanowire for which there are no analytical solutions.
© 2003 Elsevier B.V. All rights reserved.

1. Introduction

Modeling the electron states in semiconductor nanostructures remains a difficult computational task. Various computational methods such as the transfer matrix method [1], the finite element method [2], the finite difference method [3–6], and the fast Fourier transform technique [7] have been used. Other methods, the effective index method and numerical relaxation, have also been used to calculate the ground state of a cylindrical quantum dot (QD) [8]. The finite difference method (FDM) has been, by far, the most commonly used method. Nevertheless, implementation details are rarely given. One exception is in the study of GaN quantum wells by Chuang and Chang [9] and a recent paper in this journal [6]. We note, however, that they were both done in cartesian coordinates with a uniform grid. Already, in 1990, Tan et al. [3] had demonstrated that a non-uniform grid is more efficient. In addition, the recent paper by El-Moghraby et al. [6] only treated the case of a constant effective mass (i.e. same in all layers). The more realistic position-dependent effective mass leads not only to better quantitative results but also

---

* Corresponding author.
   E-mail address: llew@wpi.edu (L.C. Lew Yan Voon).

imposes a severe constraint on the accuracy of any implementation of the FDM due to the resulting discontinuity in the slope of the wavefunction.

Our work is motivated by two recent sets of papers. In the first one, most of which were published in the present journal, various authors have applied the FDM in cylindrical polar coordinates (CPC) to study quantum dots using the one-band effective mass equation [10–12], but details of the FDM were not given. In particular, complications of the formulation near the cylinder axis were not mentioned and it is, therefore, not clear how they were addressed. In the second one, there has been a flurry of experimental activity on the growth of free-standing semiconductor nanowire superlattices (NWSL's) [13,14]. These NWSL's are characterized by a cylindrical cross-section, a periodicity along the cylinder axis, and an effectively infinite potential barrier for the electrons outside the wire. Extremely polarized photoluminescence is one characteristic that makes NWSL's likely candidates for practical applications. In addition, a recent one-dimensional theory predicted the remarkable existence of an inversion regime when the localization of the electron states can be reversed [15].

Our central goal here is to demonstrate the applicability of the FDM in CPC for the novel study of NWSL's. FDM in CPC is needed since using the admitted more flexible cartesian system will lead to a three-dimensional problem rather than two-dimensional for a cylindrical cross-section. Also, we show how to solve a periodic problem and formulate the FDM in the presence of Bloch periodicity; this leads to a nonsymmetric, complex matrix eigenvalue problem. In the process, we report the correct formalism for treating the boundary condition near the cylinder axis. This theory should be helpful in solving similar problems that arise in certain other coordinate systems (such as the spherical polar one). One application of our theory is to answer the question of how many periods are required before the finite-length structure is a good approximation to the infinitely periodic structure (superlattice). We also compare the FDM to an implementation of the finite element method (FEM) using FEMLAB as a further check on the correctness of the implementation. Finally, the technique is used to confirm the existence of an inversion regime and to obtain the energy spectrum of an embedded system for which there are no analytical solutions.

2. Theory

The theory of the electron state used here is the one-band envelope function theory [6,16]. In our calculations, the effective mass of the electron is position dependent, but does not depend on energy. Non-parabolicity is not important for the systems studied, GaAs/AlGaAs nanostructures, due to the large band gap present but it can be introduced as proposed by Li et al. [10–12]. Similarly, strain can be introduced by renormalizing the effective mass and potential energy. However, we ignore both effects here in order to focus on our novel computational implementation. The task is to solve the one-electron BenDaniel–Duke equation [16],

$$\frac{-\hbar^2}{2} \nabla \cdot \left[\frac{1}{m(\mathbf{r})} \nabla \psi_n(\mathbf{r}) \right] + V(\mathbf{r}) \psi_n(\mathbf{r}) = E_n \psi_n(\mathbf{r}), \tag{1}$$

when the effective mass $m(\mathbf{r})$ and the potential $V(\mathbf{r})$ have cylindrical symmetry. The NWSL is modeled as a cylinder of infinite length, with alternating layers of GaAs (the well) and AlGaAs (the barrier) (see Fig. 1). The NWSL's currently being grown are free standing. An accurate modeling of such a structure is achieved by using an infinite potential barrier outside, where the wavefunction is, therefore, zero. In this paper, we use the term wavefunction in a loose sense to refer to the envelope function [16].

3. Computational models

Three methods are used: the finite difference method (FDM) applied to a unit cell (well + barrier) with periodic boundary conditions (PBC) (see Fig. 2(a)), the FDM applied to a finite number of unit cells (see Fig. 2(b)), and
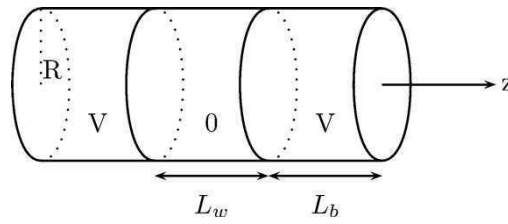
Fig. 1. A model nanowire superlattice. The parameters are: radius R, well width L_w, barrier width L_b, effective mass in the well m_w, effective mass in the barrier m_b, and the band offset V.
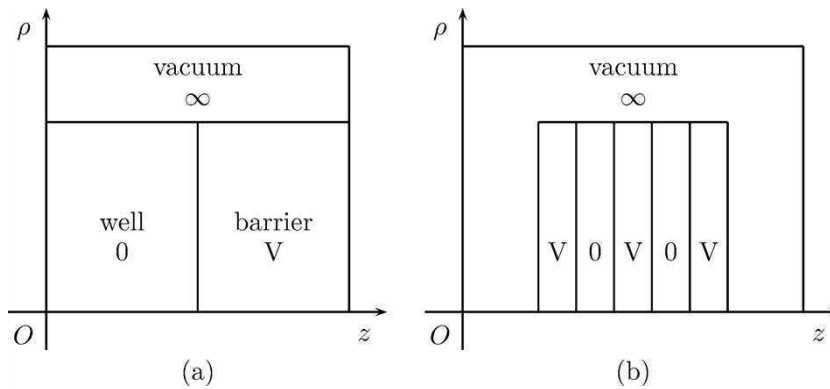

Fig. 2. The domain for (a) a unit cell with periodic boundary conditions and (b) a finite number of unit cells, with barrier layers at both ends.

the exact solution of the equivalent Kronig–Penney model. The FDM was implemented using a non-uniform grid and is two-dimensional (in the radial and z directions). When studying a finite sequence of wells and barriers, with infinite potential barriers at the ends, three patterns are possible: the ends are both wells, at one end there is a well and at the other there is a barrier, and the ends are both barriers. In the first and third case, the structure is symmetric with respect to a center plane, and the wavefunctions are symmetric or antisymmetric. In the second case, the structure is asymmetric with respect to a center plane. In the first (or second) case, the infinite potential adjacent to the wells will produce extra quantum confinement, increasing the energy of two (or one) states localized at the well-vacuum interface. The remaining eigenvalues will converge to the infinite superlattice values. The finite structures studied in this article have either two barriers at the ends, or one barrier and one well.

The FDM described in this paper can be applied to other problems, e.g., cylindrical QD's, conical QD's, and spherical QD's. The method is also suitable for analyzing electronic states in a semiconductor nanostructure embedded in a semiconductor substrate, a region of finite potential, where the wavefunction has an exponential decay. This is the situation when our FDM method is most useful, since analytical methods based on separation of variables in the BenDaniel–Duke equation do not apply.

For a planar superlattice of finite length, Kolbas and Holonyak have developed a transfer matrix method (TMM) [17]. The TMM can also be applied for a cylindrical superlattice of finite length, provided it is surrounded by vacuum. In the TMM method, the first and last barrier regions are extended to infinity, which gives a slightly different structure from the one studied here. We also note that they used an incorrect boundary condition, though this is not expected to impact the numerical convergence.
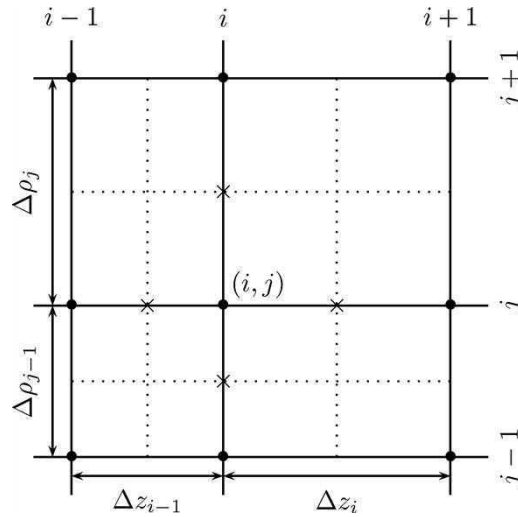
Fig. 3. Indexing of points on the non-uniform grid. • at grid points. × at midway points.

3.1. FDM applied to a unit cell with PBC

This method has the advantage of a smaller grid and, therefore, significantly reduced memory and computing time requirements. The disadvantage is the presence of complex numbers in the Hamiltonian matrix, due to the use of Bloch's theorem.

We write the gradient and the divergence operators in cylindrical coordinates. The BenDaniel–Duke equation, Eq. (1), becomes

$$\frac{-\hbar^2}{2}\left[\frac{1}{\rho}\frac{1}{m}\frac{\partial\psi}{\partial\rho} + \frac{\partial}{\partial\rho}\left(\frac{1}{m}\frac{\partial\psi}{\partial\rho}\right) + \frac{1}{\rho}\frac{\partial}{\partial\phi}\left(\frac{1}{m}\frac{1}{\rho}\frac{\partial\psi}{\partial\phi}\right) + \frac{\partial}{\partial z}\left(\frac{1}{m}\frac{\partial\psi}{\partial z}\right)\right] + V\psi = E\psi. \tag{2}$$

Due to the cylindrical symmetry, $V = V(\rho, z)$, $m = m(\rho, z)$, and $\psi = F(\rho, z)e^{iL\phi}$, where L is an integer. The BenDaniel–Duke equation becomes

$$\frac{-\hbar^2}{2}\left[\frac{1}{\rho}\frac{1}{m}\frac{\partial F}{\partial\rho} + \frac{\partial}{\partial\rho}\left(\frac{1}{m}\frac{\partial F}{\partial\rho}\right) + \frac{-L^2}{m\rho^2}F + \frac{\partial}{\partial z}\left(\frac{1}{m}\frac{\partial F}{\partial z}\right)\right] + VF = EF. \tag{3}$$

Away from the z axis, the equation is discretized the usual way. Let i label grid points along the z direction, and let j label grid points along the radial direction (see Fig. 3). With the notation $F_{i,j} \equiv F(z_i, \rho_j)$, etc., the derivatives are calculated with a central difference scheme on the non-uniform grid as

$$\frac{\partial F_{i,j}}{\partial z} = F_{i-1,j}A_i + F_{i,j}B_i + F_{i+1,j}C_i, \tag{4}$$

where

$$\begin{aligned} A_i &\equiv \frac{-\Delta z_i}{\Delta z_{i-1}(\Delta z_{i-1} + \Delta z_i)}, \\ B_i &\equiv \frac{\Delta z_i - \Delta z_{i-1}}{\Delta z_{i-1}\Delta z_i}, \\ C_i &\equiv \frac{\Delta z_{i-1}}{\Delta z_i(\Delta z_{i-1} + \Delta z_i)}, \end{aligned} \tag{5}$$

and as

$$\frac{\partial F_{i,j}}{\partial \rho} = F_{i,j-1}D_j + F_{i,j}E_j + F_{i,j+1}G_j, \tag{6}$$

where

$$
\begin{aligned}
D_j &\equiv \frac{-\Delta\rho_j}{\Delta\rho_{j-1}(\Delta\rho_{j-1} + \Delta\rho_j)}, \\
E_j &\equiv \frac{\Delta\rho_j - \Delta\rho_{j-1}}{\Delta\rho_{j-1}\Delta\rho_j}, \\
G_j &\equiv \frac{\Delta\rho_{j-1}}{\Delta\rho_j(\Delta\rho_{j-1} + \Delta\rho_j)}.
\end{aligned}
\tag{7}
$$

To avoid problems due to the discontinuous jumps of the effective mass, we expand the derivatives using midway points [18]. In this way the differential operator is applied only to the continuous functions F, $\frac{1}{m}\frac{\partial F}{\partial \rho}$, and $\frac{1}{m}\frac{\partial F}{\partial z}$. The discretized terms are

$$
\begin{aligned}
\frac{\partial}{\partial z}\left(\frac{1}{m_{i,j}}\frac{\partial F_{i,j}}{\partial z}\right) &= \frac{1}{m_{i-1/2,j}}\frac{\partial F_{i-1/2,j}}{\partial z}2A_i + \frac{1}{m_{i,j}}\frac{\partial F_{i,j}}{\partial z}2B_i + \frac{1}{m_{i+1/2,j}}\frac{\partial F_{i+1/2,j}}{\partial z}2C_i \\
&= \frac{1}{m_{i-1/2,j}}\frac{F_{i,j} - F_{i-1,j}}{\Delta z_{i-1}}2A_i + \frac{1}{m_{i,j}}\frac{F_{i+1,j} - F_{i-1,j}}{\Delta z_{i-1} + \Delta z_i}2B_i \\
&\quad + \frac{1}{m_{i+1/2,j}}\frac{F_{i+1,j} - F_{i,j}}{\Delta z_i}2C_i,
\end{aligned}
\tag{8}
$$

and

$$
\begin{aligned}
\frac{\partial}{\partial \rho}\left(\frac{1}{m_{i,j}}\frac{\partial F_{i,j}}{\partial \rho}\right) &= \frac{1}{m_{i,j-1/2}}\frac{\partial F_{i,j-1/2}}{\partial \rho}2D_j + \frac{1}{m_{i,j}}\frac{\partial F_{i,j}}{\partial \rho}2E_j + \frac{1}{m_{i,j+1/2}}\frac{\partial F_{i,j+1/2}}{\partial \rho}2G_j \\
&= \frac{1}{m_{i,j-1/2}}\frac{F_{i,j} - F_{i,j-1}}{\Delta\rho_{j-1}}2D_j + \frac{1}{m_{i,j}}\frac{F_{i,j+1} - F_{i,j-1}}{\Delta\rho_{j-1} + \Delta\rho_j}2E_j \\
&\quad + \frac{1}{m_{i,j+1/2}}\frac{F_{i,j+1} - F_{i,j}}{\Delta\rho_j}2G_j.
\end{aligned}
\tag{9}
$$

The discretized BenDaniel–Duke equation is obtained as

$$
\begin{aligned}
&F_{i-1,j}\frac{\hbar^2}{2}\left(\frac{2A_i}{m_{i-1/2,j}\Delta z_{i-1}} + \frac{2B_i}{m_{i,j}(\Delta z_{i-1} + \Delta z_i)}\right) + F_{i+1,j}\frac{\hbar^2}{2}\left(-\frac{2B_i}{m_{i,j}(\Delta z_{i-1} + \Delta z_i)} - \frac{2C_i}{m_{i+1/2,j}\Delta z_i}\right) \\
&\quad + F_{i,j-1}\frac{\hbar^2}{2}\left(-\frac{D_j}{\rho_j m_{i,j}} + \frac{2D_j}{m_{i,j-1/2}\Delta\rho_{j-1}} + \frac{2E_j}{m_{i,j}(\Delta\rho_{j-1} + \Delta\rho_j)}\right) \\
&\quad + F_{i,j+1}\frac{\hbar^2}{2}\left(-\frac{G_j}{\rho_j m_{i,j}} - \frac{2E_j}{m_{i,j}(\Delta\rho_{j-1} + \Delta\rho_j)} - \frac{2G_j}{m_{i,j+1/2}\Delta\rho_j}\right) \\
&\quad + F_{i,j}\frac{\hbar^2}{2}\left(-\frac{E_j}{\rho_j m_{i,j}} - \frac{2A_i}{m_{i-1/2,j}\Delta z_{i-1}} + \frac{2C_i}{m_{i+1/2,j}\Delta z_i} - \frac{2D_j}{m_{i,j-1/2}\Delta\rho_{j-1}} + \frac{2G_j}{m_{i,j+1/2}\Delta\rho_j} + \frac{L^2}{m_{i,j}\rho_j^2}\right) \\
&\quad + V_{i,j}F_{i,j} = EF_{i,j}.
\end{aligned}
\tag{10}
$$

Eq. (10) applies for points in the bulk of the structure. At midway points on the interfaces, the mass is calculated as an arithmetic average of the masses on the neighboring grid points. The points on the boundary of the domain require a special treatment, since Eq. (10) does not apply for points with $\rho_j = 0$, as ρ_j appears in the denominator.

A different approach is needed to determine the function $F(\rho = 0, z)$. Eq. (3) is multiplied by ρ^2, then the terms are evaluated in the limit $\rho \to 0$. We are left with $L^2 F(\rho = 0, z) = 0$. Therefore, if $L \neq 0$ then $F(\rho = 0, z) = 0$. For the case $L = 0$, Eq. (3) is multiplied by ρ, then the terms are evaluated in the limit $\rho \to 0$. We are left with $\frac{\partial F}{\partial \rho}|_{\rho=0} = 0$. The derivative calculated with a forward difference scheme on the non-uniform grid is

$$\frac{\partial F_{i,j-1}}{\partial \rho} = F_{i,j-1} \frac{-(2\Delta\rho_{j-1} + \Delta\rho_j)}{\Delta\rho_{j-1}(\Delta\rho_{j-1} + \Delta\rho_j)} + F_{i,j} \frac{\Delta\rho_{j-1} + \Delta\rho_j}{\Delta\rho_{j-1}\Delta\rho_j} + F_{i,j+1} \frac{-\Delta\rho_{j-1}}{\Delta\rho_j(\Delta\rho_{j-1} + \Delta\rho_j)} = 0. \quad (11)$$

In summary, for points with $\rho_{j-1} = 0$, if $L \neq 0$ the discretized equation is obtained from Eq. (10) with $F_{i,j-1} = 0$. If $L = 0$ the discretized equation is obtained from Eq. (10) with

$$F_{i,j-1} = F_{i,j} \frac{(\Delta\rho_{j-1} + \Delta\rho_j)^2}{\Delta\rho_j(2\Delta\rho_{j-1} + \Delta\rho_j)} - F_{i,j+1} \frac{(\Delta\rho_{j-1})^2}{\Delta\rho_j(2\Delta\rho_{j-1} + \Delta\rho_j)}. \quad (12)$$

The above treatment of Schrödinger's equation in CPC does not appear to have been previously reported. The treatment, of course, depends upon the differential equation. For example, we note that this boundary condition issue was discussed for the Navier–Stokes equation in cylindrical coordinates and a staggered grid was used in order to deal with the $\rho = 0$ axis [19].

For points with $\rho_j = \rho_{\max}$ (see Fig. 2), we apply Neumann boundary conditions: $\frac{\partial F}{\partial \rho} = 0$. The discretized equation is obtained from Eq. (10) with $M_{i,j+1/2} = M_{i,j-1/2}$ and with $F_{i,j+1} = F_{i,j-1}$. Since for bound states both the wave function and its derivative vanish at the radial edge of the computational domain, Dirichlet and Neumann boundary conditions are equivalent. It is more useful to use Neumann conditions since in this way we can check the value of the wave function on the boundary [3]. Spurious states, with energy just below the barrier but which do not vanish on the boundary, are in this way identified and discarded.

Assume that inside the domain the index i takes values from 1 to N_z. For points with $z_i = z_1$, in order to substitute for z_0 in Eq. (10), we use Bloch's theorem:

$$F(\rho, z_0) = e^{-iKZ} F(\rho, z_{N_z}), \quad (13)$$

where K is the wave number associated with the periodicity in the z direction, and the period is Z. Therefore we replace $M_{i-1,j}$ with $M_{i-1+N_z,j}$ and $F_{i-1,j}$ with $F_{i-1+N_z,j}e^{-iKZ}$. For points with $z_i = z_{N_z}$, in order to substitute for z_{N_z+1} in Eq. (10), we use Bloch's theorem again:

$$F(\rho, z_{N_z+1}) = e^{iKZ} F(\rho, z_1). \quad (14)$$

Therefore we replace $M_{i+1,j}$ with $M_{i+1-N_z,j}$ and $F_{i+1,j}$ with $F_{i+1-N_z,j}e^{iKZ}$.

3.2. FDM applied to a finite number of unit cells

This method applies well to semiconductor nanostructures of finite length, e.g., quantum dots. It has the advantage that only real numbers appear in the Hamiltonian matrix. However, for large structures, memory requirements can be a problem. The periodic structure of the NWSL is generated by a finite sequence of unit cells (well + barrier). The discretized equation and boundary conditions are as discussed previously, with the exception of the points with $z = 0$ or $z = z_{\max}$. These points are in the vacuum layer; in order to be able to use the same program for structures embedded in a semiconductor substrate (i.e. finite barrier), we do not use Dirichlet boundary conditions. Bound states are then easily authenticated, by inspection of the magnitude of the wavefunction on the boundary [3].

For points with $z = 0$ (see Fig. 2) we apply Neumann boundary conditions: $\frac{\partial F}{\partial z} = 0$. The discretized equation is obtained from Eq. (10) with $M_{i-1/2,j} = M_{i+1/2,j}$ and with $F_{i-1,j} = F_{i+1,j}$. For points with $z = z_{\max}$ we apply Neumann boundary conditions: $\frac{\partial F}{\partial z} = 0$. The discretized equation is obtained from Eq. (10) with $M_{i+1/2,j} = M_{i-1/2,j}$ and with $F_{i+1,j} = F_{i-1,j}$.

4. Equivalent Kronig–Penney model

In order to validate our computational models, we now obtain the exact solutions, only possible when the outside layer is vacuum. We solve Eq. (3) by separation of variables, with $F(\rho, z) = J(\rho)Z(z)$. We also use the fact that, for the NWSL under investigation, $m = m(z)$ and $V = V(z)$. Solution of the decoupled radial equation gives $J(\rho) = J_L(\rho q)$, where q is the separation constant and J_L is the cylindrical Bessel function of order L. The separation constant q is determined by the condition that Rq be a zero of the Bessel function. The decoupled equation for z is [15]

$$\frac{-\hbar^2}{2}\frac{\partial}{\partial z}\left(\frac{1}{m}\frac{\partial Z}{\partial z}\right) + \left(V + \frac{\hbar^2 q^2}{2m}\right)Z = EZ. \tag{15}$$

This equation describes a Kronig–Penney model with a potential $V_{eq:KP} = V + \hbar^2 q^2/2m$. We increase the origin of the energy by $\hbar^2 q^2/2m_w$, such that the potential in the well is zero and in the barrier is $V' = V + \hbar^2 q^2/2m_b - \hbar^2 q^2/2m_w$. Eq. (15) is solved by writing the wavefunctions in the well and in the barrier, and then imposing the matching boundary conditions for the functions and their derivatives [20]. When writing the boundary conditions, we use Bloch's theorem and introduce the quantum number K. We are left with a system of four linear homogeneous equations. A zero determinant is obtained only when

$$\cos\left[K(L_w + L_b)\right] = \cos(k_w L_w)\cos(k_b L_b) + \frac{k_b^2 m_w/m_b - k_w^2 m_b/m_w}{2k_w k_b}\sin(k_w L_w)\cos(k_b L_b), \tag{16}$$

where $k_w \equiv \sqrt{2m_w E'}/\hbar$ and $k_b \equiv \sqrt{2m_b(V' - E')}/\hbar$. The energy of the NWSL is given by $E = E' + \hbar^2 q^2/2m_w$. The transcendental equation (Eq. (16)) is solved numerically. In summary, four indices label the energy eigenvalues: the angular momentum number L, an index N to label the roots $q_{L,N}$ of the Bessel function, the quantum number K due to the translational periodicity in the z direction, and an index M to label the roots of the transcendental equation (Eq. (16)).

5. Results and discussions

A representative set of parameters used for the calculations were as follows: radius $R = 100$ Å, well (L_W) and barrier (L_B) widths of 50 Å, well (m_W) and barrier (m_B) effective masses of $0.067m_0$ and $0.0919m_0$, and a barrier height of 0.23 eV. These parameters correspond to a GaAs/Al$_{0.3}$Ga$_{0.7}$As structure [7]. In the radial direction the infinite barrier extended for 10 Å. When modeling a finite lattice, two 10 Å wide regions of infinite potential were used to pack the structure in the z direction. In practice the infinite potential is approximated by 10^6 eV, and a region of finite dimension is needed to allow the exponentially decaying wave function to vanish. Free standing NWSL's have been grown [13], and the complete localization of electrons inside these NWSL's justifies our approximation of infinite surrounding potential.

We used a non-uniform grid with a grid step varying from 1 Å to 0.025 Å (see Fig. 4). The non-uniform grid is used at the interfaces, and also near the z axis. No grid point lies on the well-barrier interface, where the effective mass is discontinuous. The total number of grid points is $140 \times (40 + 70N)$ for the non-uniform grid, and
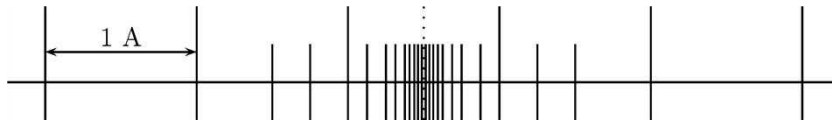

Fig. 4. Detailed structure of the non-uniform grid at the well-barrier interface. Grid steps of 1, 0.5, 0.25, 0.125, 0.0625, 0.03125, and 0.025 Å are used.
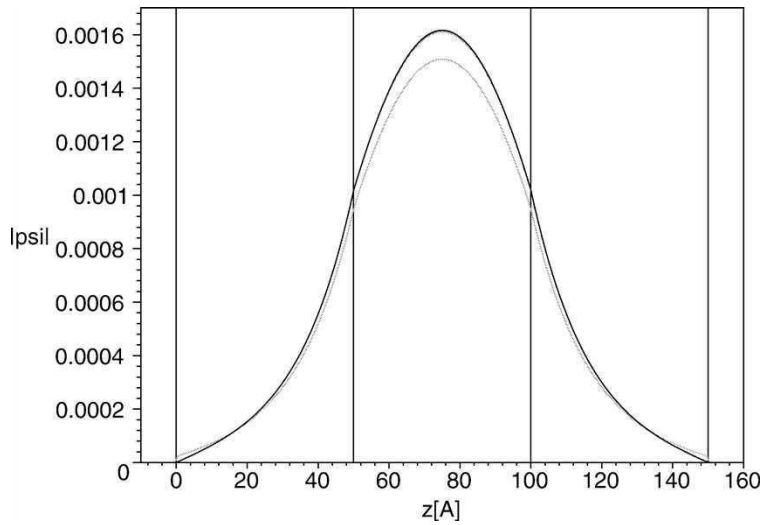
Fig. 5. Ground state for the NWSL calculated with the FEM (dotted black curve), the FDM with uniform grid (solid gray curve), the FDM with non-uniform grid (dotted gray curve), and the equivalent Kronig–Penney model (solid black curve).

$110 \times (20 + 50N)$ for the uniform grid, where N is the number of semiconductor layers. A simple uniform grid (of 1 Å) could not reproduce the discontinuous jump of the derivative of the wavefunction at the well-barrier interface. This discontinuity, due to the abrupt change in the effective mass, has dramatic effects; in particular, it validates the Heisenberg uncertainty principle [21].

A calculation using the finite element method (FEM) has also been performed, using FEMLAB. The FEM is a variational reformulation of the problem, so we do not need to treat the interfaces in any special way. The FEM solves partial differential equations (PDE) in weak form by integrating the PDEs. Thus slope discontinuities are captured, as calculations reveal, and one can get the correct result even with a fairly sparse grid. In Fig. 5 we have plotted a cross section, at $\rho = 0.5$ Å, of the ground-state wavefunction of the simplest barrier-well-barrier structure. The FEM calculation overlaps perfectly over the exact solution, the FDM calculation with non-uniform grid is also very accurate, while the FDM calculation with uniform grid but with about the same number of total grid points is not very good, due to the poor grid around the interfaces. As a practical calculational detail, the wavefunctions have been normalized to unit cell: $\int_\Omega |\psi|^2 \rho \, d\rho \, d\theta \, dz = 1$. In contrast, the eigenvector resulted from the numerical procedure is normalized as $\sum_{i,j} |\psi_{i,j}|^2 = 1$.

The eigenvalue problem for the large sparse matrix was solved using ARPACK [22]. The LU decomposition, external to the ARPACK library, has been performed with UMFPACK. On a computer with 2 GB RAM running at 2 GHz, the computation took from a few seconds to a few minutes. Results for the electron energies obtained using the above methods are given in Figs. 5–9. The FDM provided the energy eigenvalues with an error $< 0.5\%$. In Figs. 6 and 7 we study finite NWSL structures, with barrier layers at both ends and, respectively, with one barrier and one well layer at the ends. We find that the finite-length NWSL structure with barrier layers at both ends approaches the superlattice energy bands when the number of unit cells is of the order of 6. Note, however, that the infinite NWSL (with PBC) reproduces the exact solution (given on the right-hand side) a lot faster.

The miniband formation in Fig. 6 can be understood from a perturbative point of view. Indeed, consider the case of barriers of length much larger than the wells. In this situation the wells are practically decoupled, and in each one we have the eigenstates of the single well. As the length of the barriers is decreased, the states interact more strongly with each other, and their energies shift, forming the miniband. It is clear that the number of states in one miniband is equal to the number of wells in the superlattice structure. Each energy level of the single well will correspond to a miniband in the infinite superlattice structure. The miniband formation in Fig. 7 can be
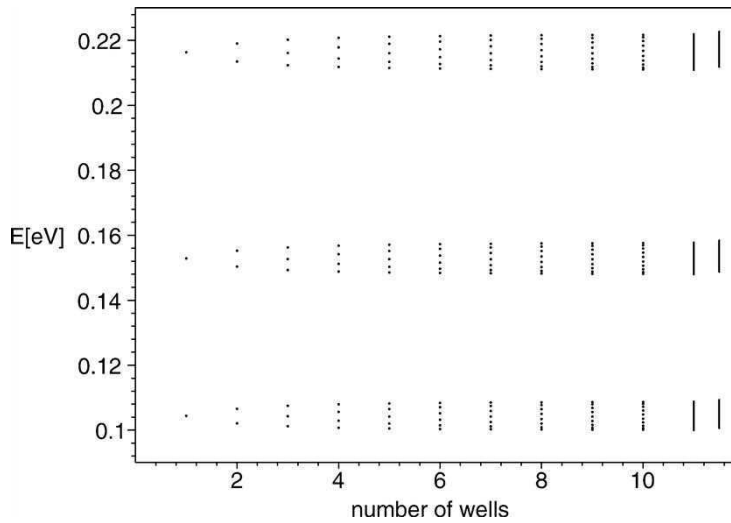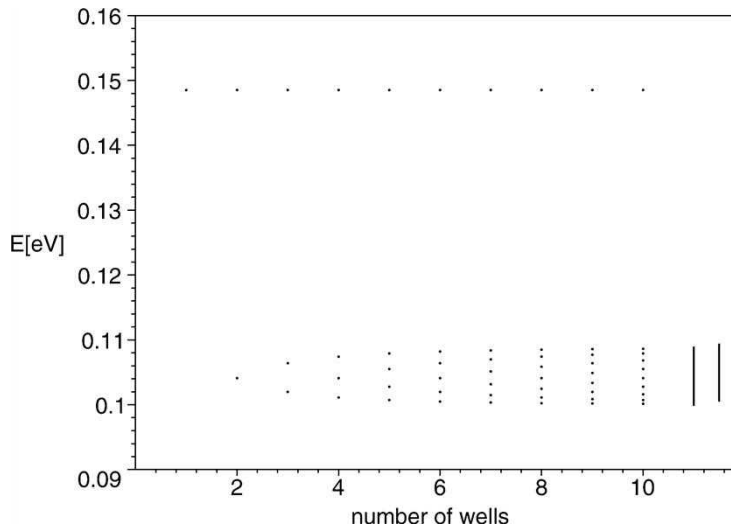
Fig. 6. Miniband formation in a symmetric NWSL structure. Energy levels as a function of the number of wells. The segments on the right side are the energy bands for the infinite NWSL, calculated with the FDM with non-uniform grid (left segments) and with the equivalent Kronig–Penney model (right segments). $L = 0$, $L = 1$, and $L = 2$, in increasing order of the energy.

Fig. 7. Miniband formation in an asymmetric NWSL structure. Energy levels as a function of the number of wells. The segments on the right side are the energy bands for the infinite NWSL, calculated with the FDM with non-uniform grid (left segments) and with the equivalent Kronig–Penney model (right segments). $L = 0$.

understood in the same way. Here, however, the state localized at the well-vacuum interface is higher in energy, due to the increased quantum confinement, and does not mix with the other states in the miniband. A similar state sandwiched between AlGaAs and vacuum does not exist in the symmetrical structure (Fig. 2(b)).

The lowest set of points on the left-hand side of Fig. 6, lying between 0.10 eV and 0.11 eV, corresponds to the solutions with quantum numbers $L = 0$, $N = 1$, $M = 1$. In fact, they are the discretized version of the miniband present in the superlattice calculation, shown in Fig. 8. The clustering of the levels towards the top and bottom of a miniband can be readily explained in terms of the density of states of the miniband. As shown in Fig. 8, at the
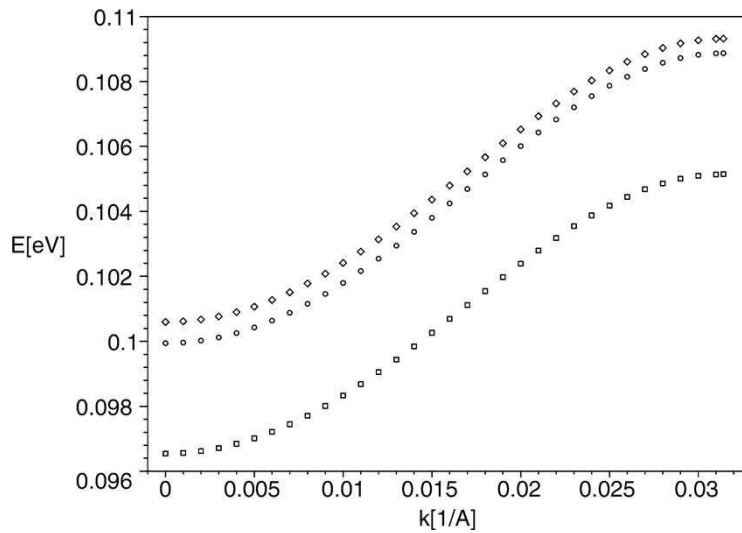
Fig. 8. An energy band in the first Brillouin zone, calculated using the FDM with uniform grid (squares, lowest curve), the FDM with non-uniform grid (circles, middle curve), and the equivalent Kronig–Penney model (diamonds, upper curve). The quantum numbers are $L = 0$, $N = 1$, $M = 1$.
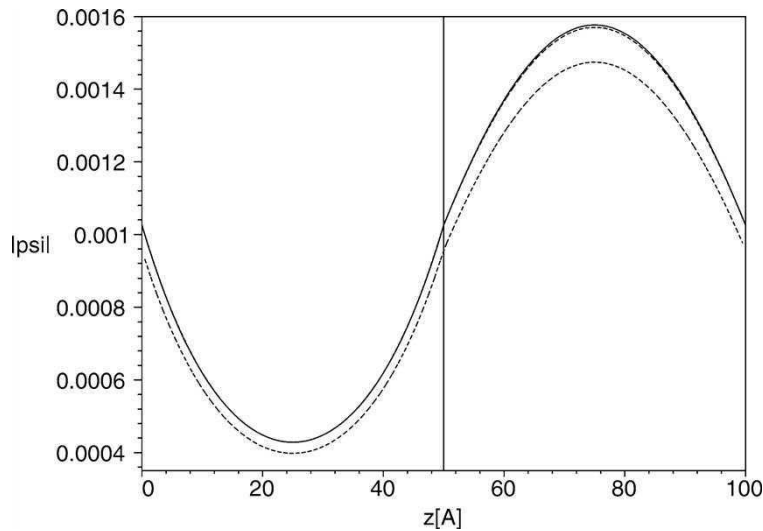

Fig. 9. Ground state for the NWSL calculated with the FDM with uniform grid (lower dotted curve), the FDM with non-uniform grid (upper dotted curve), and the equivalent Kronig–Penney model (solid curve).

top and bottom of a miniband the derivative $\partial E/\partial K$ is at a minimum, and therefore the number of states N in an energy interval $\partial N/\partial E = (\partial N/\partial K)/(\partial E/\partial K)$ is at a maximum.

In Fig. 9, we show a cross section, at $\rho = 0.5$ Å, of the NWSL ground-state wavefunction. The wavefunction $|\psi|$ plotted clearly shows the discontinuity of its derivative, due to the change in the effective mass at the well-barrier interface. The success of the FDM calculation with non-uniform grid is now clear from the excellent agreement of both the eigenvalue and the eigenfunction. The deficiencies of the FDM calculation with uniform grid (of 1 Å)

are also apparent. The uniform grid has failed to provide an accurate solution even in the simpler one dimensional calculation of Tan et al. [3].

6. Physical applications

6.1. Inversion

In Ref. [15], the authors predicted the existence of a critical radius for NWSL's, below which the role of well and barrier layers are reversed. This result followed directly from the exact one-dimensional Kronig–Penney equation. However, this approach does not allow for an *ab initio* verification from the localization of the wave function. This would require a full two-dimensional solution without assuming the existence of the critical radius. We have carried this out using our FDM program. Thus, the eigenvalue problem was solved for a small radius. From the Kronig–Penney model, the critical radius is expected to be around 20 Å. We, therefore, did a calculation for a radius of 18 Å, though we expect some correction of the quantitative data to be necessary at this small radius due to the approximations of the physical model of a parabolic band [10–12].

The resulting ground state wavefunction is given in Fig. 10 (a cross-section at $\rho = 0.5$ Å). The localization of the wavefunction in the $Al_{0.3}Ga_{0.7}As$ layer (to the left) is clear (solid curve). This is compared to the localization of the wavefunction in the GaAs layer for the much larger radius (dashed curve). Thus, the numerical method is able to reproduce the correct wave function localization, a much more sensitive test than just getting the right energies. The difference in the vertical scale of the two functions is due to the much larger localization of the electron along the wire axis for the small radius. This is also a result not obtained within the one-dimensional exact model. Finally, we note that being able to get the correct wavefunction is a prerequisite for calculating optical and transport properties.
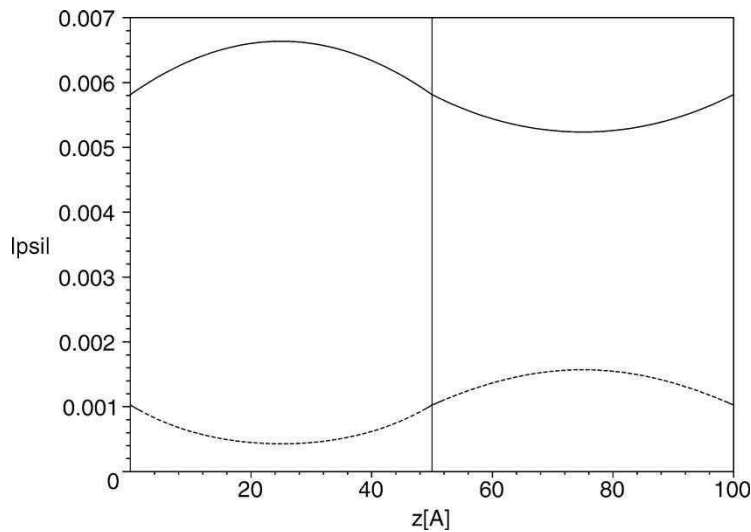

Fig. 10. Ground state for the NWSL calculated with the FDM with non-uniform grid for a radius of 18 Å (solid curve) compared to a radius of 100 Å (dashed curve). The left (right) layer is AlGaAs (GaAs).
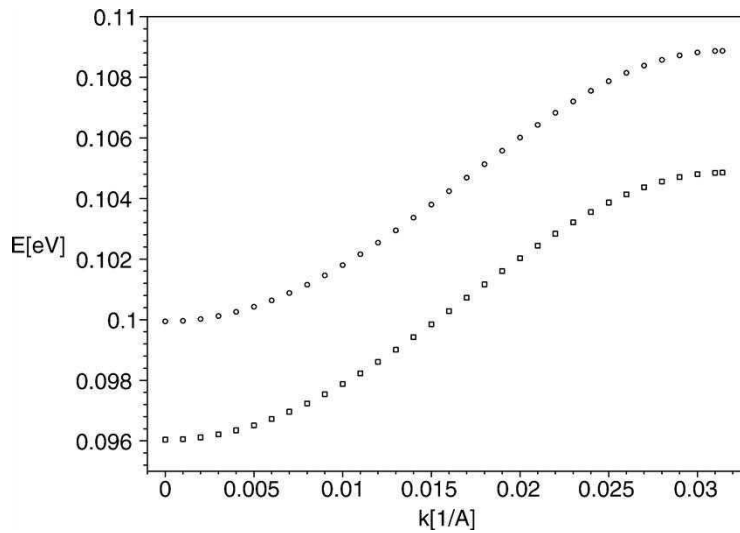
Fig. 11. Lowest energy band in the first Brillouin zone for a finite outside barrier $V = 1.878$ eV (squares, lower curve) compared to an infinite barrier one (circles, upper curve). The structure is the same in both cases (radius of 100 Å).

6.2. Embedded nanowire

As a final example of a possible application of the new technique, we now consider a nanowire embedded in another semiconductor material. We can simulate this with AlAs outside the wire. Note that embedded NWSL's have not yet been grown. However, embedded quantum wires had been actively grown in the past [23]. This problem is of interest because, for this physical system, there are no analytical solutions. Hence, the use of a numerical technique such as the FDM is necessary.

In the current calculation, we set the outside barrier height to be 1.878 eV and the effective mass to be $0.1m_0$ (pure AlAs). The grid in the z direction is the same as before for the infinite barrier problem. In the radial direction, we now have a dimension of 100 Å for the NWSL (i.e. same radius of 100 Å as before), and a width of 310 Å for the AlAs layer. The grid in the radial direction is 10 Å at 1 Å grid step, 100 Å at 2 Å, and 200 Å at 4 Å. Note that it is not necessary to have too many points in the outside barrier since the wavefunction decays exponentially there. In Fig. 11, we give the resulting energy band (lower curve) compared to the infinite barrier result obtained earlier (upper curve). As expected, it is lower than with an infinite barrier outside due to the reduced quantum confinement. For this particular structure, the band is more or less uniformly lower by about 4%. We are, therefore, in a position to calculate the energies and wavefunctions of any NWSL, free standing or embedded, within the one-band model. Our algorithm should be better suited and much more efficient than the one recently proposed by El-Moghraby et al. [6] for NWSL's.

7. Conclusions

The theory of the finite difference method in cylindrical polar coordinates and with periodic boundary conditions (together with a non-uniform grid and a position-dependent mass) is given in detail. In particular, the implementation of the boundary condition on the cylinder axis is clarified. Applications to finite-length and infinite-length structures show that, for a finite NWSL with barrier layers at both ends, only about six unit cells are necessary in approximating the energy bands of a periodic system. However, the use of the Bloch theorem speeds up the solution of the latter problem and reduces the memory requirements. Verification of our two-dimensional

computational model was achieved by comparing with one-dimensional exact results. We then used the model to obtain a numerical proof of the possible existence of inverted states without any a priori assumptions. New results were also obtained for the case of an embedded nanowire for which there are no exact solutions.

Acknowledgements

References

[1] A.K. Ghatak, K. Thyagarajan, M.R. Shenoy, IEEE J. Quantum Elec. 24 (1988) 1524.
[2] K. Nakamura, A. Shimizu, M. Koshiba, K. Hayata, IEEE J. Quantum Elec. 25 (1989) 889.
[3] I.-H. Tan, G.L. Snider, L.D. Chang, E.L. Hu, J. Appl. Phys. 68 (1990) 4071.
[4] L.C. Lew Yan Voon, M. Willatzen, Semicond. Sci. Technol. 10 (1995) 416.
[5] M. Tsetseri, G.P. Triberis, Superlattices and Microstructures 32 (2002) 79.
[6] D. El-Moghraby, R.G. Johnson, P. Harrison, Comput. Phys. Comm. 150 (2003) 235.
[7] D.L. Mathine, S.K. Myjak, G.N. Maracas, IEEE J. Quantum Elec. 31 (1995) 1216.
[8] G. Lamouche, Y. Lépine, Phys. Rev. B 51 (1995) 1950.
[9] S.L. Chuang, C.S. Chang, Semicond. Sci. Technol. 12 (1997) 252.
[10] Y. Li, J.-L. Liu, O. Voskoboynikov, C.P. Lee, S.M. Sze, Comput. Phys. Comm. 140 (2001) 399.
[11] Y. Li, O. Voskoboynikov, C.P. Lee, S.M. Sze, Comput. Phys. Comm. 141 (2001) 66.
[12] Y. Li, O. Voskoboynikov, C.P. Lee, S.M. Sze, Solid State Comm. 120 (2001) 79.
[13] M.S. Gudiksen, L.J. Lauhon, J. Wang, D.C. Smith, C.M. Lieber, Nature 415 (2002) 617.
[14] R. Solanki, J. Huo, J.L. Freeouf, B. Miner, Appl. Phys. Lett. 81 (2002) 3864.
[15] L.C. Lew Yan Voon, M. Willatzen, J. Appl. Phys. 93 (2003) 9997.
[16] G. Bastard, Wave Mechanics Applied to Semiconductor Heterostructures, Halsted Press, Paris, 1988.
[17] R.M. Kolbas, N. Holonyak Jr., Am. J. Phys. 52 (1984) 431.
[18] P. Harrison, Quantum Wells, Wires and Dots, Wiley, New York, 1999.
[19] R. Verzicco, P. Orlandi, J. Comput. Phys. 123 (1996) 402.
[20] H.-S. Cho, P.R. Prucnal, Phys. Rev. B 36 (1987) 3237.
[21] L.C. Lew Yan Voon, Superlattices and Microstructures 31 (2002) 269.
[22] D.C. Sorensen, C. Yang, Arpack User's Guide, SIAM, 1998.
[23] E. Kapon, D.M. Hwang, R. Bhat, Phys. Rev. Lett. 63 (1989) 430.